Cell Reports
Physical Science

CellPress

Article

In Operando Acoustic Detection of Lithium Metal Plating in Commercial $LiCoO_2$/Graphite Pouch Cells

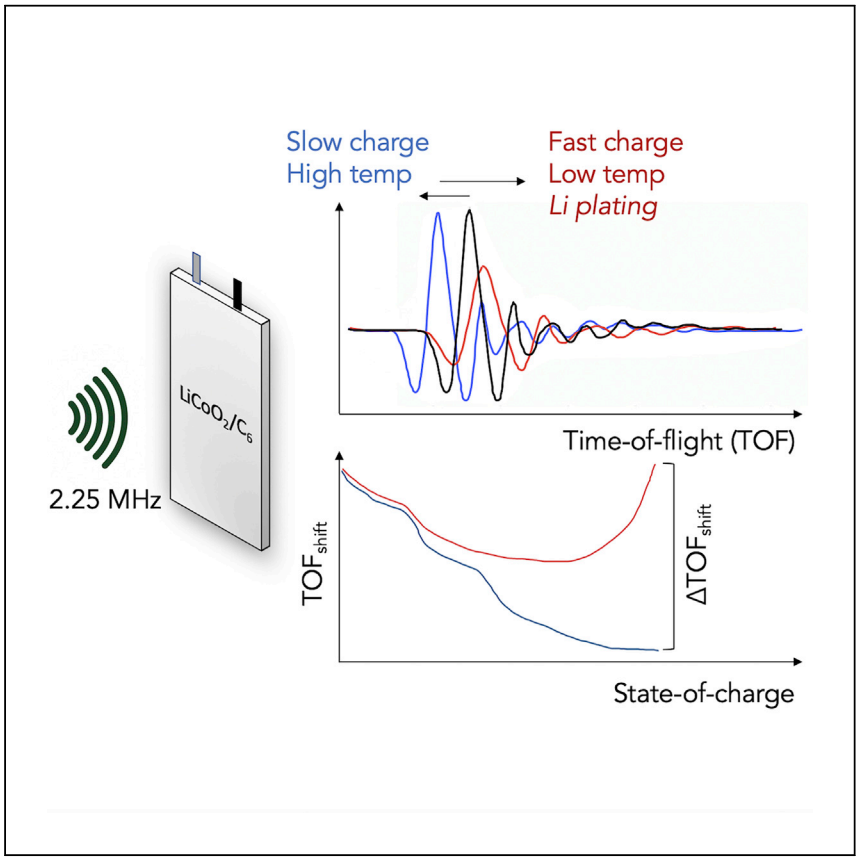

Unfavorable lithium metal plating in commercial Li-ion batteries is known to occur at colder temperatures and faster charge rates. Bommier et al. apply a commercially applicable ultrasonic technique to determine the degree of lithium metal plating during battery cycling as a function of temperature and charge rate.

Clement Bommier, Wesley Chang, Yufang Lu, ..., Robert Mohr, Mateo Williams, Daniel Steingart

dan.steingart@columbia.edu

HIGHLIGHTS

Ultrasonic signals can detect lithium metal plating in commercial Li-ion batteries

Degree of plating determined by measuring differences in ultrasonic time of flight

28 combinations of charge rate and temperature conditions mapped out

Plating occurrence confirmed *post mortem*, ultrasonic technique is rapid and simple

Bommier et al., Cell Reports Physical Science *1*, 100035
April 22, 2020
https://doi.org/10.1016/j.xcrp.2020.100035

Cell Reports
Physical Science

CellPress

Article

In Operando Acoustic Detection of Lithium Metal Plating in Commercial $LiCoO_2$/Graphite Pouch Cells

Clement Bommier,[1,2,4,7] Wesley Chang,[1,2,6,7] Yufang Lu,[1,2] Justin Yeung,[1,2] Greg Davies,[1,2] Robert Mohr,[5,6] Mateo Williams,[5,6] and Daniel Steingart[1,2,3,4,5,6,8,*]

SUMMARY

The characterization and detection of lithium metal plating during standard operation of commercial Li-ion batteries has been a long-term challenge; the nature of lithium metal plating is unpredictable and highly dependent on operating temperature and charge rate. *In operando* detection of lithium plating is critical for ongoing and future developments of conventional Li-ion batteries, including fast charging capabilities, extreme temperature applications, and lithium metal secondary batteries. In this study, we describe the use of acoustic ultrasound to detect lithium metal plating on commercial graphite anodes within a standard form factor. Extending from previous work on ultrasound as a battery diagnostic tool, this proof-of-concept study delineates statistically significant linear relationships between ultrasonic time-of-flight and graphite staging, and acoustic time-of-flight and *post mortem* electrochemical measurements to characterize the extent of lithium metal plating.

INTRODUCTION

A primary mode of Li-ion battery (LIB) degradation is the loss of Li inventory due to localized plating reactions coupled with solid-electrolyte-interphase (SEI) formation on the graphite anode.[1–5] These unwanted side reactions cause significant losses in state of health (SOH) over the lifetime of the battery and are exacerbated by a combination of higher charging rates and lower operational temperatures. However, extending LIB operational conditions to higher charging rates and wider temperature ranges is highly sought after, as it may further increase the scope of their applications.[6–9] To accomplish this, it is important to better understand electrochemical structure-property relationships of LIBs as a function of operating temperature and rate capability. An improved ability to detect localized Li metal plating reactions stemming from higher charging rates and/or lower operational temperatures will aid in this endeavor.

Historically, non-destructive methods for detecting localized Li metal plating in LIBs have been challenging to set up. An elegant and straightforward method is to correlate cell thickness measurements with plating, *in operando*.[10,11] Although this is a proven method, it is unable to distinguish between gassing reactions and Li metal plating, which may both increase cell thickness. Analysis of the electrochemical behavior, such as coulometry,[12,13] voltage curve analysis,[14–20] or calorimetry,[21] also offers insight but relies on average measurements of the entire cell and often conflates plating- and non-plating-related side reactions.[22] For example, Uhlmann et al. attributed plating to an inflection point in the voltage transients.[19] Many of

[1]Department of Mechanical and Aerospace Engineering, Princeton University, Princeton, NJ 08540, USA

[2]Andlinger Center for Energy and the Environment, Princeton University, Princeton, NJ 08540, USA

[3]Department of Chemical and Biological Engineering, Princeton University, Princeton, NJ 08540, USA

[4]Department of Earth and Environmental Engineering, Columbia University, New York, NY 10027, USA

[5]Department of Chemical Engineering, Columbia University, New York, NY 10027, USA

[6]Columbia Electrochemical Energy Center, Columbia University, New York, NY 10027, USA

[7]These authors contributed equally

[8]Lead Contact

*Correspondence: dan.steingart@columbia.edu

https://doi.org/10.1016/j.xcrp.2020.100035

these electrochemical approaches also confirm plating via optical or scanning electron microscope (SEM) imaging.

Direct detection of Li metal through chemical/structural analysis is also possible but often requires a destructive *post mortem* approach. Furthermore, typical characterization techniques have associated difficulties. Energy dispersive X-ray spectroscopy (EDX) is unable to detect the weak X-ray signal of Li metal. X-ray photoelectron spectroscopy (XPS) provides ambiguous peak deconvolution of the low binding energy Li species and destructively interferes with the reactive surface. Electron microscopy can image dendrites growing on the surface but does not provide information on their chemical composition or when they initiate during cycling. The most effective technique seems to be ^{7}Li NMR (nuclear magnetic resonance spectroscopy), which exhibits a distinct peak directly correlated to Li metal.[23–26] Neutron diffraction is also a proven method of detecting Li metal *in operando*.[27,28] However, both ^{7}Li NMR and neutron diffraction necessitate specially customized equipment that may not be readily accessible by typical electrochemical research labs. Specifically, neutron diffraction indirectly detects Li metal via the LiC_{12} and LiC_6 peaks. For these reasons, the most facile and scalable detection method for Li metal plating is best done with an indirect measurement method, coupled with a more thorough *ex situ* analysis to corroborate the findings.[29,30]

Previous work by Hsieh et al. introduced the ability of acoustic ultrasound to probe physical dynamics of a battery during cycling.[31] Specifically, Davies et al.[33] attributed the shifts in the transmitted ultrasonic signals due to variations of the electrode density and bulk modulus. Similarly, Gold et al.[32] utilized a comparably lower frequency ultrasonic pulse (~200 KHz versus 2.25 MHz) to analyze the arrival time of the slow, compressional wave. This work demonstrates that the simple and scalable *in operando* acoustic technique can be utilized to detect Li metal plating in commercial-scale LIBs. The detection method is semiquantitative, as more significant Li metal plating results in increased hysteresis of the acoustic time of flight. The acoustic technique can observe localized and heterogeneous plating events, because the signal comes from the total acoustic pathway between the locations on the cell connected to the transducers. Moreover, the technique can be deployed with minimal start-up costs, requiring transducers, an acoustic detector, and an open source software package.[33–35] As will be shown in the manuscript, this method for detecting lithium metal plating is much more expedient for commercial cells, bypassing the need to disassemble the entire cell and observe/characterize each individual electrode for plating.

Using insight gathered from the *in operando* acoustic measurements, we are able to delineate an Arrhenius relationship between Li metal plating, current rate, and operating temperature, as well as show the dependence on state of charge of Li metal plating. Specifically, statistically significant linear relationships are discovered to exist between the ultrasonic time of flight and degree of graphite staging and between the ultrasonic time of flight and *post mortem* electrochemical measurements. This work serves to further prove the robustness of the *in operando* acoustic method and also to provide researchers another framework with which to approach operational characteristics of LIBs within the parameters of current rate and temperature.

RESULTS AND DISCUSSION

Acoustics and Voltage-Dependent Cycling Protocol

Initial attempts to detect Li metal plating *in operando* consisted of cycling commercial 210-mAh Li-ion cells using a combination of 5°C temperatures coupled with

higher current rates. Such low-temperature and high-rate conditions are known to be favorable for Li metal plating reactions on the graphite electrode.[31,36,37]

To ensure the graphite was completely delithiated prior to the charge step, an asymmetrical cycling protocol was used, with a C/10 discharge rate followed by a faster charge rate. Cold temperatures are favorable for but do not necessarily induce Li metal plating, especially in cases of incomplete charging. This was previously demonstrated in a paper by Carter et al.,[38] who showed that, in strictly cold conditions, Li metal plating did not readily occur due to constricted Li transport, leading to an inability to reach full state of charge (SOC). As such, it was necessary to create a thermal gradient with a cold interface at the graphite surface and a warm interface at the cathode side to allow for ample mass transfer of Li. This led to optimal plating conditions. However, establishing a temperature gradient with the acoustic setup would be difficult and may potentially convolute the acoustic waveform, which is strongly affected by temperature. The asymmetrical charge/discharge protocol, making use of a constant current constant voltage charge (CCCV) and a slow constant current (CC) discharge, seemed like the optimal way to enable plating kinetics at the interface while maximizing mass transfer—which could be throttled due to incomplete delithiation of the anode on the discharge step.

Unfortunately, the initial asymmetrical cycling protocol did not provide conclusive results. As opposed to obtaining a difference in the acoustic time-of-flight (TOF) shift, the predominant response was the attenuation of the acoustic signal. This is well demonstrated in Figure 1A, where a consistent acoustic signal is seen in the first two slow C/10 cycles, only to be attenuated upon the first 1C CCCV charge (around t = 35 h). In the subsequent asymmetrical cycles of fast charge and slow C/10 discharge, the capacity drops precipitously, from 0.18 Ah to below 0.10 Ah within 20 cycles, suggesting that plating is in fact occurring and leading to capacity losses (Figure S1A).

Although an argument could be made relating the loss of the acoustic signal to plating, this is problematic for two reasons. For example, acoustic signal can be lost to gassing, which was one of the issues with volume/thickness measurement techniques for Li metal plating: they have difficulty distinguishing between gassing and plating, which this acoustic technique is attempting to resolve. In fact, loss of acoustic signal is a strong indicator of gassing, as the transmission efficiency from transducer to air is much lower than that from transducer to liquid, due to a greater impedance mismatch ratio.[39]

Furthermore, the loss of acoustic signal at low temperatures/high current rates is not necessarily permanent. In Figure 1B, a 210-mAh cell undergoes a similar protocol of asymmetric fast charge/slow discharge. As with the other cell, it quickly loses the acoustic signal, this time within the second cycle (around t = 20 h). However, the signal reappears briefly 18 cycles later (around t = 195 h). Although this could be a case for Li metal plating, the drop in capacity is not nearly as steep, with a starting capacity of 0.210 Ah that only decreases to 0.195 Ah after 20 cycles (Figure S1B). The variation between these results, with different capacity outcomes and the brief reappearance of the acoustic signal for the second cell (Figure 1B), shows that using acoustic attenuation alone as a basis for Li metal plating is ineffective.

Second, this method is limited by the cycling protocol. Because full lithiation necessitates a CCCV charge, higher current rates tend to hit the 4.2-V cutoff earlier on in the charging process, so that the remainder of the charging process occurs at

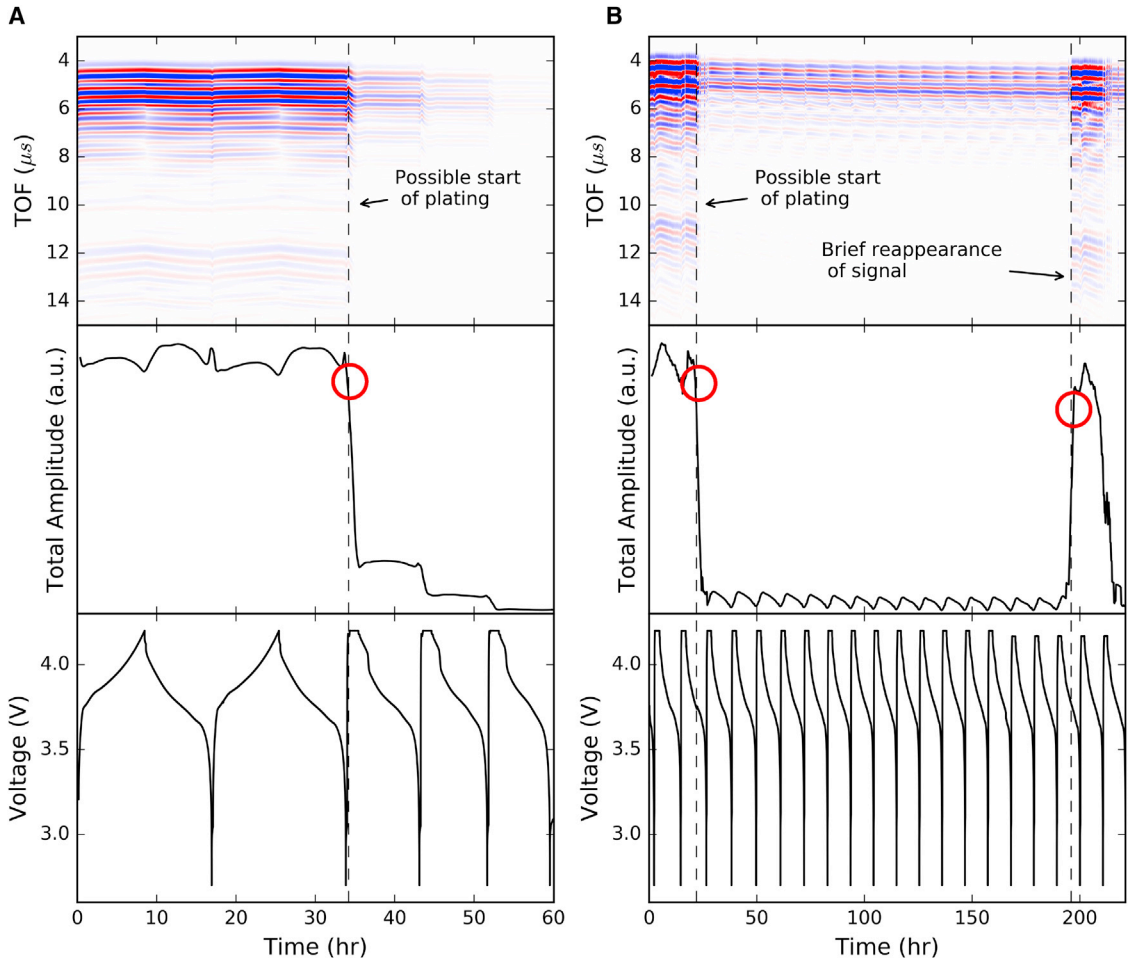

Figure 1. Acoustics and Voltage-Dependent Cycling Protocol

Acoustic plots consisting of three panels: (top of panel) heatmap of acoustic time of flight (μs), with individual waveforms collated with respect to time, (middle of panel) total amplitude of waveforms in arbitrary units, and (bottom of panel) voltage versus time curve corresponding with the adjoined waveforms.

(A) Acoustic results of a 210-mAh cell cycled at 5°C, for two cycles at a C/10 CC charge and discharge, followed by cycles of 1C CCCV charge and C/10 CC discharge. The acoustic signal quickly attenuates and then disappears upon the first 1C CCCV charge, which is ascribed to the possible start of Li metal plating.

(B) 210-mAh cell cycled at 5°C using a 1C CCCV charge and C/10 CC discharge. The acoustic signal is lost on the second cycle before reappearing on the 18th cycle and disappearing shortly thereafter. The signal travels from the transmitting transducer to the receiving transducer (see also Figure S4 for schematic of acoustic detection technique).

progressively lower current rates. This variability in the charge current rate fails to provide complete insight into the plating process, especially if the plating is most prevalent at higher SOCs, because a CCCV charge would be utilizing lower currents at a high SOC. Switching to a CC charge is also not a solution, as complete lithiation would not be attained, which would also limit conclusions on the plating process.

Acoustics of "Fixed Capacity" Charging

Due to issues with characterizing plating through signal attenuation with a CCCV charge, we decided to instead measure shifts in the full acoustic waveforms. The acoustic TOF shift is defined here as the change in the time of arrival of the wave as the cell is cycled. Changes in the material properties of the cell components, such as Li intercalation into graphite or Li plating on the surface, cause the ultrasonic

wave to propagate through the cell at varying speeds. A cross-correlation function was used to calculate the time shift by comparing the full waveform shapes.

Under the new method, cells were cycled twice at a current rate of C/15 for both charge and discharge. This allowed for the establishment of the expected TOF shift profile, with minimal risk of signal loss due to plating or electrolyte side reactions. Following the initial two slow cycles, a "plating charge" would be applied, which is defined to be a CC charge with a capacity cutoff of 0.21 Ah and no voltage cutoff. Using a capacity cutoff ensures that a full lithiation will take place. The acoustic correlation with side reactions or Li metal plating due to overpotentials above specified operating conditions is not viewed as a shortcoming of this fixed capacity cutoff but rather as a feature: it enables us to probe the performance limitations of the battery without having to deal with issues, such as incomplete charging.

This second protocol provided insightful results. The first set of tests was done in a 10°C environment under four different C rates: 0.5C, 0.75C, 0.88C, and 1C. From Figure S2A, it can be observed for the 0.5C rate condition that the first two C/15 cycles show a clear TOF shift, with the TOF decreasing during the charging step and increasing during the discharge step. This agrees with results from Davies et al.,[33] who attributed the TOF shift decrease on charge to the increasing stiffness of the graphite anode. Because the graphite has a larger volumetric-specific capacity than $LiCoO_2$ (LCO), it takes up a larger portion of the acoustic pathway and will have a greater impact on the TOF. Having established the dominant effect of the graphite anode in this case, we speculate that the local inflection points in the TOF shift may be due to graphite staging events, as these are located at the same SOC as inflection points in the voltage curve. When the bottom of charge is taken as the reference point (see red circle in Figure S2A), the TOF initially decreases with the nadir located close to the top of charge, before recovering back to the original position after discharge. The TOF shifts for the initial slow C/15 charge and the faster fixed capacity charge were compiled for all tests and analyzed. As described in Figure 2A, the acoustic TOF shift between the C/15 current rate (blue curve) and the 0.5C fixed capacity charge (red curve) is similar. However, as the current rate is increased to 0.75C and 0.88C, the respective TOF shift between the slow charge and the faster fixed capacity charge begins to deviate (Figures 2B and 2C). At the current rate of 1C, there is a clear anomaly that develops within the cell at around 0.070 Ah: the initially decreasing TOF shift suddenly reverses course and starts to increase. When the fixed capacity charge is finished, the TOF shift is completely different from that of the C/15 charge, with a large difference in the endpoints (Figure 2D).

These results indicate the possibility of using the TOF endpoint difference as a plating detection parameter. To further validate that gassing and temperature have relatively minimal effects on the TOF endpoint difference, Figure S3 demonstrates effects due to gassing and temperature. With a pouch cell that had undergone visible gassing and swelling, the permanent attenuation of the acoustic signal can be observed (Figure S3B). As discussed earlier, acoustic waveforms are known to propagate much more easily through solid or liquid mediums due to a lower impedance mismatch ratio, and significant attenuation of the signal implies the presence of gassing. As there was no evidence of gassing or signal attenuation in the 10°C cells, a plating event points itself as the most likely culprit. A complete study on the effect of cell gassing on acoustic signals can be found in a separate referenced report.[40]

The acoustic signal is also known to be sensitive to environmental temperature. Utilizing a thermistor placed directly on the 210-mAh pouch cell during cycling

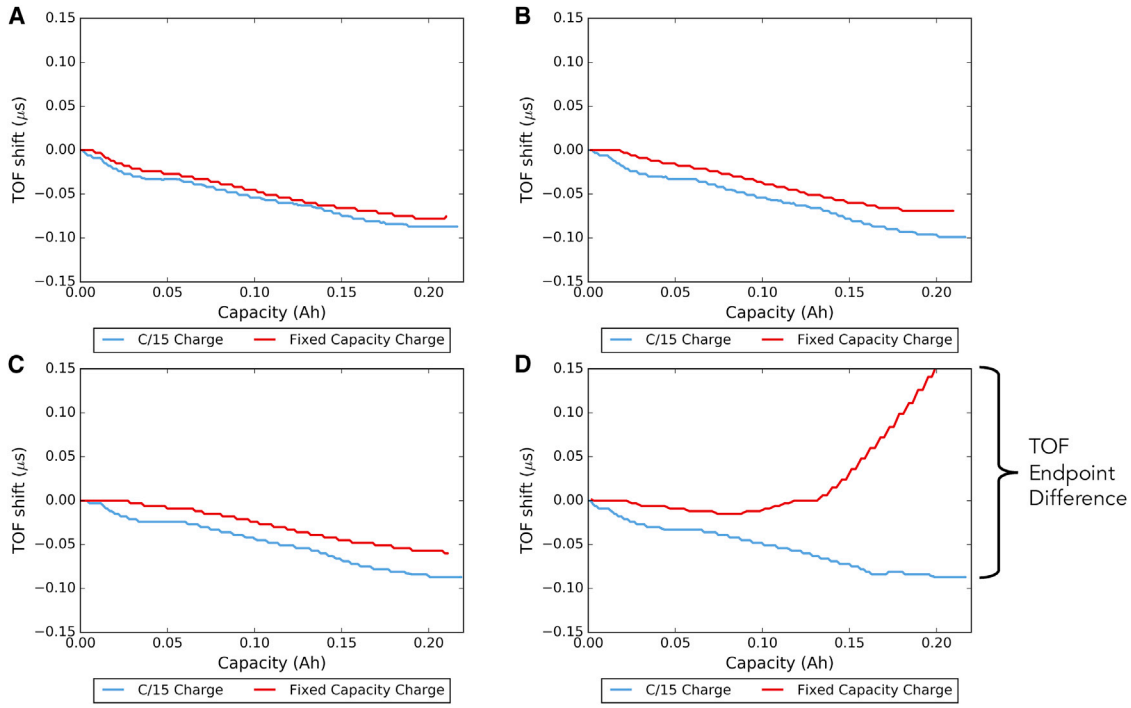

Figure 2. Acoustics of Fixed-Capacity Charging

Comparison of acoustic TOF shifts during the C/15 charge and the fixed-capacity charge of 0.210 Ah, at four different current rates. No voltage cutoffs were set for fixed-capacity charges. These cells were cycled at 10°C with a fixed capacity charge of (A) 0.5C, (B) 0.75C, (C) 0.875C, and (D) 1C. Detailed acoustic data for the 0.5C and 1C conditions are shown in Figure S2, and the method for determining acoustic TOF shift is in Figure S4. Additional details on each of the 10°C cells are in Figures S10–S13.

protocol, the surface temperature of the cell was monitored. It can be observed that there are no observable changes in temperature during the slow C/15 rate, though an increase of a few degrees Celsius can be observed during the faster charge. After the charge finishes, the cell quickly cools back to the baseline environmental temperature. Comparing the temperature changes with the acoustic signals, we notice a discrepancy. For a non-plating condition, such as 0.5C rate at 10°C, the TOF shift relaxes back to its initial position (see third subplot of Figure S2A). However, for a plating condition, such as 1C rate at 10°C, the TOF endpoint remains high relative to the initial position, despite resting for many hours. It does not downshift (see third subplot of Figure S2B), even though the cell temperature does (Figure S3A). This is one reason why we believe that, although temperature may have an effect on the shape of the acoustic waveforms due to their sensitivity, there is a less significant effect on the TOF endpoint difference. The permanent hysteresis of the TOF endpoint difference points to a permanent change in the battery as observed by *ex situ* analysis—Li metal plating on the graphite anode. In addition to the temperature relaxation after charge, the rise in the temperature of a few degrees Celsius during the fast charge may induce thermal expansion, thus increasing the acoustic path length and causing an increase in the TOF shift. This thickness increase due to thermal expansion may be estimated from the thermal expansion coefficients of the electrodes. Assuming linear expansion of an effectively isotropic material, the following equation can be used for a first-order approximation: $\Delta L/L_0 = \alpha\Delta T$. For lithium cobalt oxide, a coefficient of thermal expansion of 1.3×10^{-5}/°C and temperature increase of 4°C as measured by the thermistor results in a thickness increase of 0.0052%.[41] For graphite, a coefficient of thermal expansion of 20×10^{-6}/K results in a thickness

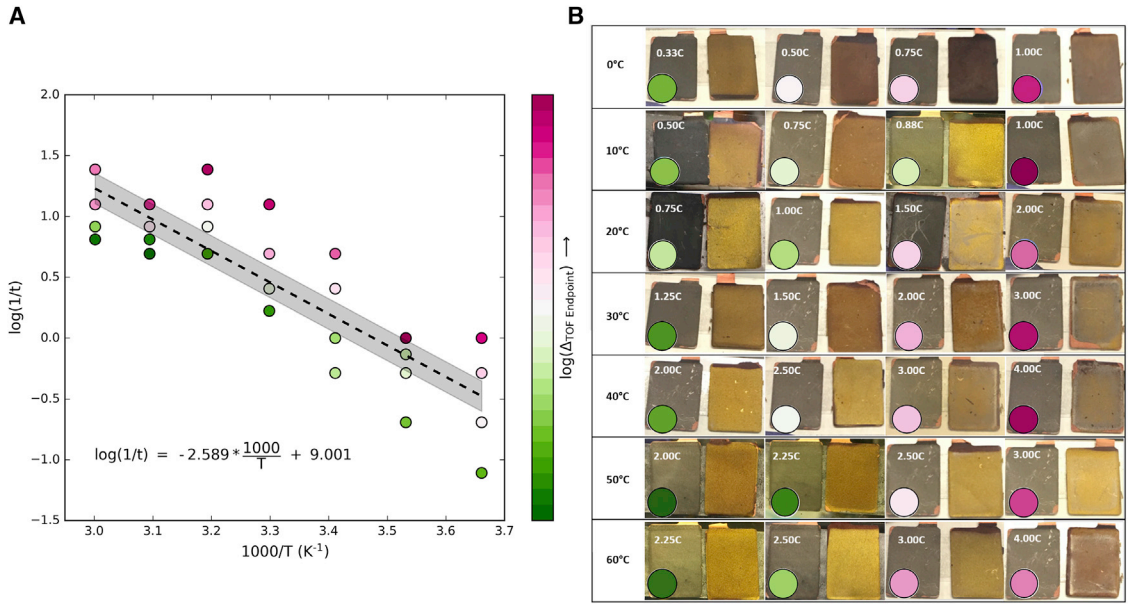

Figure 3. Arrhenius Relationship between Plating, Charge Rate, and Temperature

(A) Plot of logarithmic rate (1/t) versus inverse temperature (1,000/T), using the associated color bar to factor in the time of flight (TOF) endpoint difference between the C/15 charge and the fixed capacity charge. A symmetric logarithmic color bar has been used for easier identification of TOF endpoint differences. Lower TOF endpoint differences are indicated by an increasingly dark green color, and higher TOF endpoint differences are indicated by an increasingly dark magenta color. The depicted equation represents the linear fit (Arrhenius relationship) between logarithmic rate and inverse temperature, shown by the dotted line. The gray error bar represents the statistical standard error, which is the variance of the dataset divided by the set size. TOF endpoint differences generally increase with rate at any given temperature, as visualized by the color of the datapoint. Because plating is a continuum event, the linear fit generally describes conditions where plating is likely (i.e., one standard deviation above the linear fit) but does not conclude with certainty the presence of plating due to the statistical nature of this experiment.

(B) Optical images of a delithiated graphite anode control (left of image) and the anode at the corresponding fixed-capacity charge (right of image). The colored dot represents the TOF endpoint difference according to the color bar used in (A). Additional data on each C rate and temperature condition are in Figures S6–S33, with description of all supplemental figures in Figure S5.

increase of 0.6%.[42] Based on thermal expansion coefficients, graphite swells more than LCO, but the approximate thickness increase due to thermal expansion is still an order of magnitude lower than the ~10% thickness increase due to lithiation/delithiation. For this reason, the increase in the acoustic path length due to thermal expansion is insignificant compared with changes due to lithiation/delithiation.

A suite of similar measurements to the 10°C cells was done at temperatures ranging from 0°C to 60°C in 10°C steps, using four different current rates at each temperature. TOF endpoint differences were calculated, and cells after the fixed capacity charge were transferred to the glovebox before being disassembled at full SOC for *post mortem* characterization (Figure 3; details in Figures S6–S33 with explanation of supplemental figures in Figure S5).

Plotting logarithmic rate versus inverse temperature, with the color bar representing the TOF endpoint difference between the C/15 charge and the fixed capacity, uncovers an Arrhenius-like relationship with a correlation coefficient of 74% (Figure 3A). Operation at higher temperatures results in higher current rates needed to induce Li metal plating. Although this was expected and has been discussed in prior literature, the use of acoustic measurements, along with the fixed capacity charge technique, affords direct and semi-quantifiable measurement of plating *in operando*. As the TOF endpoint difference is directly correlated with the current rate and temperature conditions that lead to plating, the degree of plating for each condition can be

estimated from *ex situ* methods and then statistically correlated with a TOF endpoint difference value.

Optical images of the anodes in Figure 3B show a shift from the golden-colored graphite, which is representative of the LiC_6 intercalation compound, to a black/gray anode surface with a varied degree of plating. Some anodes still show the golden color but have small gray deposits, especially along the edges, which is consistent with models of Li metal plating on graphite due to edge effects.[43] Examples of this include 20°C—1.5C (Figure S16), 30°C—2C (Figure S20), 40°C—3C (Figure S24), and 50°C—3C (Figure S29) anodes. In cases of more severe plating, the deposits work their way inward from the edges and the golden color takes on a much grayer hue. This is the case for the 30°C—3C (Figure S21), 40°C—4C (Figure S25), and 60°C—4C (Figure S33) cells. Lastly, there are two examples of complete plating, where the entire anode surface is covered with a gray film and there is no golden color that can be observed. This is the case of the 0°C—1C (Figure S9) and 10°C—1C cells (Figure S13). The TOF endpoint differences from acoustic measurements mirror these results, with heavily plated anodes experiencing larger differences—thus demonstrating the strength of this method. There is a stronger correlation between TOF endpoint differences and plating as compared with the ambiguous results from the initial method utilizing attenuation signals from fully lithiated cells. It must be noted that the electrodes used for optical images were typically taken from the middle of the stack, and effort was taken to ensure the one selected was representative of a majority of the electrodes. The delithiated anode reference (left image) was simply shown for comparison in the same captured photo, because each electrode was captured at a different time with different lighting/angle.

The optical images confirm the trend seen in the TOF endpoint differences. Anode tabs that are of golden colors have lower TOF endpoint differences. The anodes that are mostly golden with a few gray/silver deposits have slightly higher TOF endpoint differences, although those covered with a gray film have the highest TOF endpoint differences. Acoustically measured TOF endpoint differences can accurately distinguish between varying degrees of plating (significant plating versus moderate plating versus insignificant plating). Moreover, acoustic detection foregoes the need for complete cell disassembly for visual observation, as the TOF measurement is representative of the entire cross section of the electrode stack. This may be why there are certain discrepancies between the optical images and the TOF endpoint difference. The plating observed on one layer may not be representative of the entire stack. Further, optical images are difficult to analyze precisely, as they are subject to how the photo was taken, though this is why a reference delithiated anode is shown next to the lithiated anode for comparison in the same captured photo. Juxtaposing the optical images with the TOF endpoint differences shows the ambiguity of simple visual evidence of plating, which should be supported by a diagnostic technique, such as acoustic signals.

Confirmation of Plating through *Ex Situ* XRD Studies

Qualitative optical images of plating were supplemented with *ex situ* XRD (X-ray diffraction) to estimate the degree of Li plating from graphite staging ratios and then correlated with the acoustic measurements. Because all 210-mAh cells had roughly the same capacity at a C/15 charge and all were subjected to a fixed capacity charge with the same amount of Ah, the degree of graphite lithiation should be the same. As such, we surmised that, as discrepancies arose, they would be due to lithiation inefficiencies, which would likely come in the form of Li metal plating.

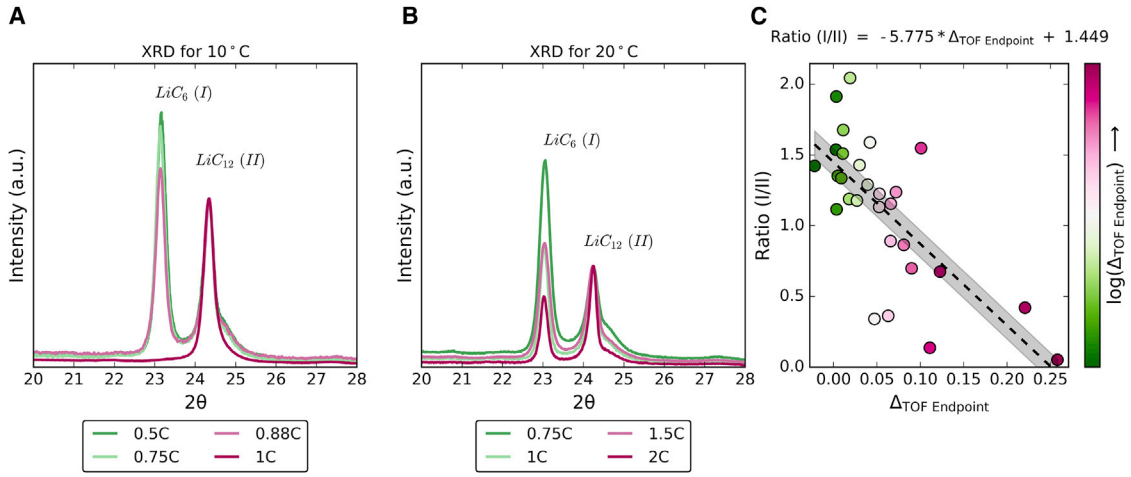

Figure 4. Confirmation of Plating through *Ex Situ* XRD Studies

(A) XRD measurements of the 10°C anodes, centered on the (002) peak.

(B) XRD measurements of the 20°C anodes.

(C) Linear regression of the stage I/stage II ratio as a function of TOF endpoint difference. The linear regression has a p value of 2.35×10^{-5}. Peak intensities were normalized according to stage II peak intensity in order to show the relative change in the peak ratios. The gray error bar represents the standard error, which is the variance of the dataset divided by the set size.

In prior diffraction studies, the phases of graphite have been ascribed to phase 1′, which happens at a stoichiometry of less than $Li_{0.04}C_6$; stage IV, which lasts until $Li_{0.125}C_6$; stage III, which goes to $Li_{0.2}C_6$; stage II, which ends at $Li_{0.8}C_6$; and lastly, stage I at LiC_6.[44–48] This translates to XRD (002) 2θ peak values of roughly 27° to 26° for phase 1′, 26° to 25.5° for stages IV and III, 25.5° to 24.5° for stage II, and 24.5° to 23.5° for stage I.[49]

The XRD results of the anodes subjected to the fixed capacity charge at 10°C (Figure 4A) exhibit stage I and stage II peaks at 23° and 24.2°, respectively. The ratio of the stage I to stage II peak intensities changes with current rate. At lower current rates of 0.50C and 0.75C, the I/II ratio was 1.51 and 1.43, respectively. As the current rate was increased to 0.88C, the ratio dropped to 1.18, and at 1C, where a major plating event occurred, the stage I peak had disappeared. The XRD results for 20°C show similar trends (Figure 4B). Therefore, increased plating activity, as determined by the TOF endpoint difference and by visual *ex situ* inspection, results in a lower degree of graphite lithiation. When the I/II ratios were plotted as a function of TOF endpoint difference, the data exhibited a downward trend and yielded a p value of 2.35×10^{-5} and R^2 of 50.4% when fitted with a simple linear regression (Figure 4C). Unfortunately, the correlation between degree of graphite staging and TOF endpoint difference is not as strong as between temperature/C rate/TOF endpoint difference, but the general trend is still observed. Graphite staging is also not linearly related to capacity passed and cannot be directly correlated with plating in any case.

Confirmation of Plating through Li Metal Half-Cell Measurements

The XRD ratios provide a good start to the quantification process, but they still lack the ability to point out exactly how much lithium (in Ah or g) was plated during the plating charge, as peak intensity ratios are not directly correlated with amount lithiated or delithiated. Therefore, *post mortem* electrochemical analysis of the disassembled pouch cells was also conducted, with the harvested graphite anodes cycled in coin cells against a Li metal counter electrode (750 μm; Sigma-Aldrich) in 1M $LiPF_6$

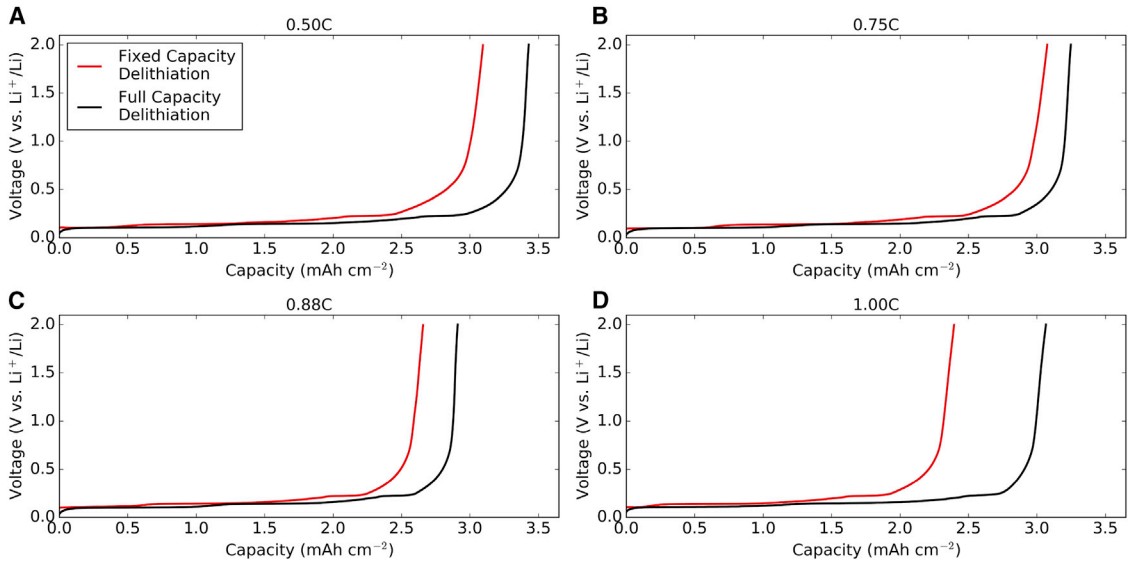

Figure 5. Confirmation of Plating through Li Metal Half-Cell Measurements

Voltage versus areal capacity plots of fixed capacity delithiation and full-capacity delithiation for the graphite anodes from the 10°C cells cycled at (A) 0.50C, (B) 0.75C, (C) 0.875C, and (D) 1.00C. The delithiation ratio is obtained by dividing the capacity from the fixed-capacity delithiation curve (red) by the full-capacity delithiation curve (black).

EC:DMC. This allowed for a semiquantitative estimation of the amount of Li metal plated, based on the total capacity that can be extracted from the graphite.

A slow delithiation at 40 μA cm^{-2} (approximately C/200) was performed to determine the amount of Li that could be extracted from the anode following the fixed capacity charge. This was followed by a slow lithiation/delithiation to determine how much Li could be delithiated following a full lithiation from a Li metal counter electrode (Figure 5). For the sake of brevity, the ratio of the delithiation following the fixed-capacity lithiation in the full cell to that of the full-capacity delithiation in the half-cell is termed the "delithiation ratio" in the next section.

A low delithiation ratio indicates that the fixed capacity charge could be the result of two events: (1) an overbuilt anode, in which the anode never had the chance to fully lithiate during the fixed capacity charge, or (2) inefficiencies where a large portion of the Li inventory failed to intercalate the graphite and was lost (e.g., plating). Meanwhile, a high delithiation ratio indicates that the fixed capacity charge was very efficient in fully lithiating the graphite and that little plating occurred.

The delithiation ratios are between 0.9 and 1.0 for most cells, indicating that the fixed capacity charge was highly efficient and did not lead to large inventory losses (Figure 6). From reverse-engineering the commercial cell, it was discovered that the anode is slightly overbuilt, with approximately 6.5% more capacity. The samples that showed heavy evidence of plating from both visual and acoustic observations, such as 0°C—1C (Figure S9), 10°C—1C (Figure S13), 30°C—3C (Figure S21), 40°C—4C (Figure S25), and 60°C—4C (Figure S33), showed significantly lower delithiation ratios. This is most likely due to the fact that those fixed-capacity charges resulted in copious amounts of "dead Li" on the anode surface, resulting in an incomplete graphite lithiation. However, when paired against an unlimited Li supply and a very slow current (~C/200), the anodes were able to reach their full lithiation potential, which had been severely underserved by the fixed-capacity charge.

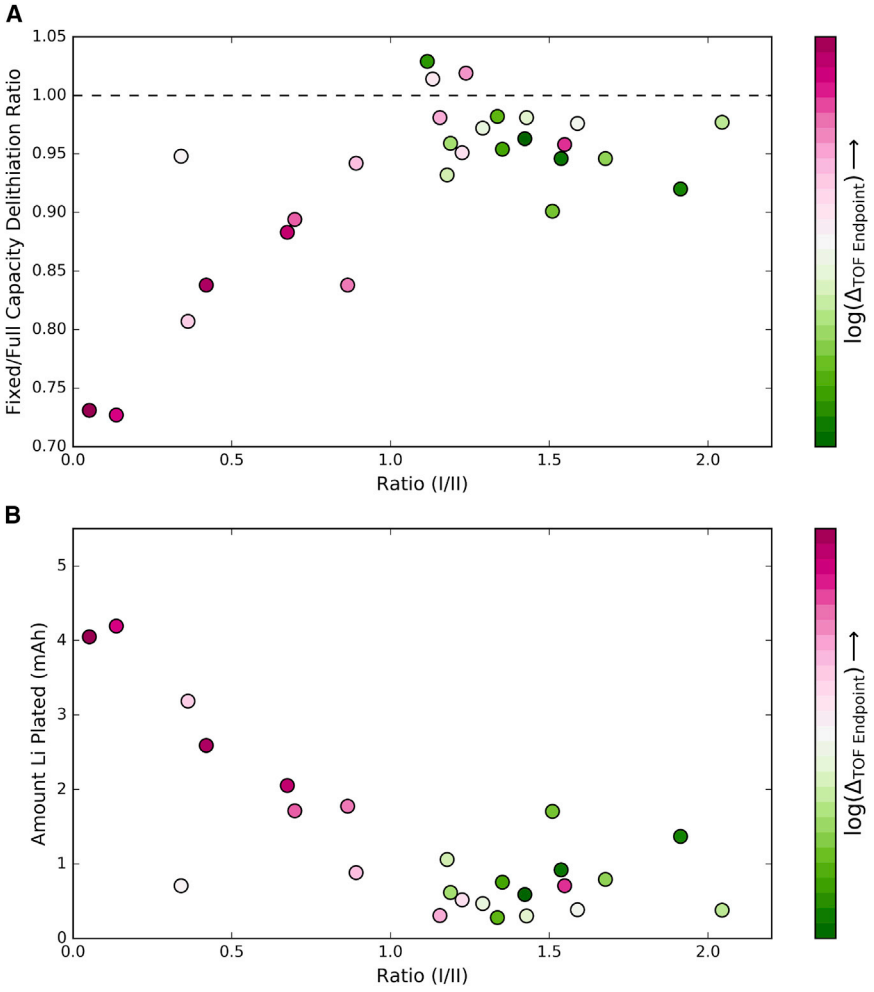

Figure 6. Acoustic Correlation of Li Metal Plating

(A) Plot of delithiation ratio versus staging ratio. The plot is linear for the lower delithiation ratios/staging ratios but then plateaus out and even regresses slightly at higher staging ratios.

(B) Plot of amount of Li plated per electrode layer (mAh) as a function of staging ratio and TOF endpoint difference, with a p value of 1.4×10^{-4}. The amount of Li plated is calculated from the difference between the delithiation capacities from the half-cell measurements and extrapolated for the entire electrode area.

A pattern emerges from the plot of the delithiation ratio versus the stage I/stage II ratio. At the low end, there is a linear relationship between delithiation ratios and staging ratios: as the staging ratios increase, so do the delithiation ratios (Figure 6A). However, this linear relationship plateaus out around the staging ratio of 1.0–1.5, even decreasing slightly for staging ratios greater than 1.5. Additionally, the delithiation ratios greater than 1.0 are all within the 1.0–1.5 range of staging ratios. At first glance, this seems illogical: the highest staging ratios should have the most complete lithiation, and as such, they should also have the highest delithiation ratios. We speculate that the higher voltages toward the end of the fixed capacity charge in more aggressive cycling rates may cause greater SEI formation and explain the lower staging ratio. The subsequent side reactions during the fixed-capacity delithiation may explain the high delithiation ratio. With Li metal plated on the surface, parasitic side reactions may occur more readily due to the increased volatility of the surface chemical species.

The delithiation ratio metric was used to estimate the total amount of Li plated (mAh) per electrode layer. Assuming that the difference between the amount initially delithiated and the amount delithiated after a slow full lithiation is equivalent to the lost amount of Li that had been plated on the surface, Figure 6B provides an estimated semiquantitative relationship between the amount of Li plated and the graphite staging ratio and TOF endpoint difference. The cells with the most amount of Li plated tend to have higher TOF endpoint differences. It should be noted that the cells with less than 1 mAh calculated amount of Li plated probably did not experience any plating, as observed optically and with the low TOF endpoint differences. The discrepancy arises from the delithiation ratio, which never reaches 1.0 due to the graphite anode being slightly overbuilt by 6.5%. Upon further statistical analysis, the correlation between the amount of Li plated and staging ratio has a p value of 1.4×10^{-4}. This is consistent with the prior visual observations and XRD measurements, which show that higher TOF endpoint difference was linked to increase in plating, further validating the developed acoustic technique as a reliable way of gauging Li metal plating in the cell.

Proof of Concept into Li Metal Plating Mechanism

To further confirm that the deviation of the TOF shift between C/15 charge and the fixed-capacity charge (as depicted in Figure 2) was due to Li metal plating, cells were charged to various SOCs under a condition that led to heavy Li metal plating (0°C at 1C rate; see also Figure S9). Following each partial capacity charge to 1/12, 1/6, 1/2, and 3/4 of full capacity, the cells were disassembled for XRD characterization (Figure 7A) and half-cell cycling of the graphite anodes (Figures 7B–7F).

The XRD spectra of the graphite anodes indicate that the (002) graphite peak gradually shifts toward lower values of 2θ as the anode is increasingly lithiated (to 5 min, 10 min, and 30 min; Figure 7A).

The delithiation curves and the extrapolated full-capacity values (scaled linearly) tell a similar story. For partial-capacity charges of 10 min and 30 min, the extrapolated full capacity is close to that of the full delithiation capacity, thus showing that the initial charging scales linearly (Figures 7C and 7D). The 5-min plot has a very limited amount of capacity passed, which may have resulted in larger error (Figure 7B). For the 45-min plot (Figure 7E), the extrapolated capacity regresses to a lower value, indicating some inefficiencies have crept into the process. For the 60-min plot (Figure 7F), the delithiation ratio regresses further, showing that more inefficiencies followed between 45 and 60 min. This is again consistent with plating activity: if the Li is not intercalating into the graphite, it must be going elsewhere and is likely engaging in irreversible plating reactions. The TOF endpoint difference (Figure 7G) is large, which suggests a significant amount of Li plating, as indicated by the correlative linear relationships described earlier. We emphasize the parameter of TOF endpoint difference being critical in detecting plating, though the TOF shift curve itself may incorporate convoluted effects, such as cell temperature and bulk modulus changes at different C rates. Although the correlations between TOF endpoint difference and estimated degree of plating from half-cell measurements and graphite staging are statistically significant, the full quantification of when plating initiates requires further refinement of the acoustic technique. As a proof of concept, this study indicates that plating may be detected as a gradual and non-linear event starting from the bottom of charge, using the TOF shift differences. To probe the origins of the TOF shift differences, fast Fourier transform (FFT) mapping was done to break down the contributions to the TOF shift in the frequency domain. From a comparison of a non-plated and a plated cell in Figures S2A and S2B, the main 2.5-MHz

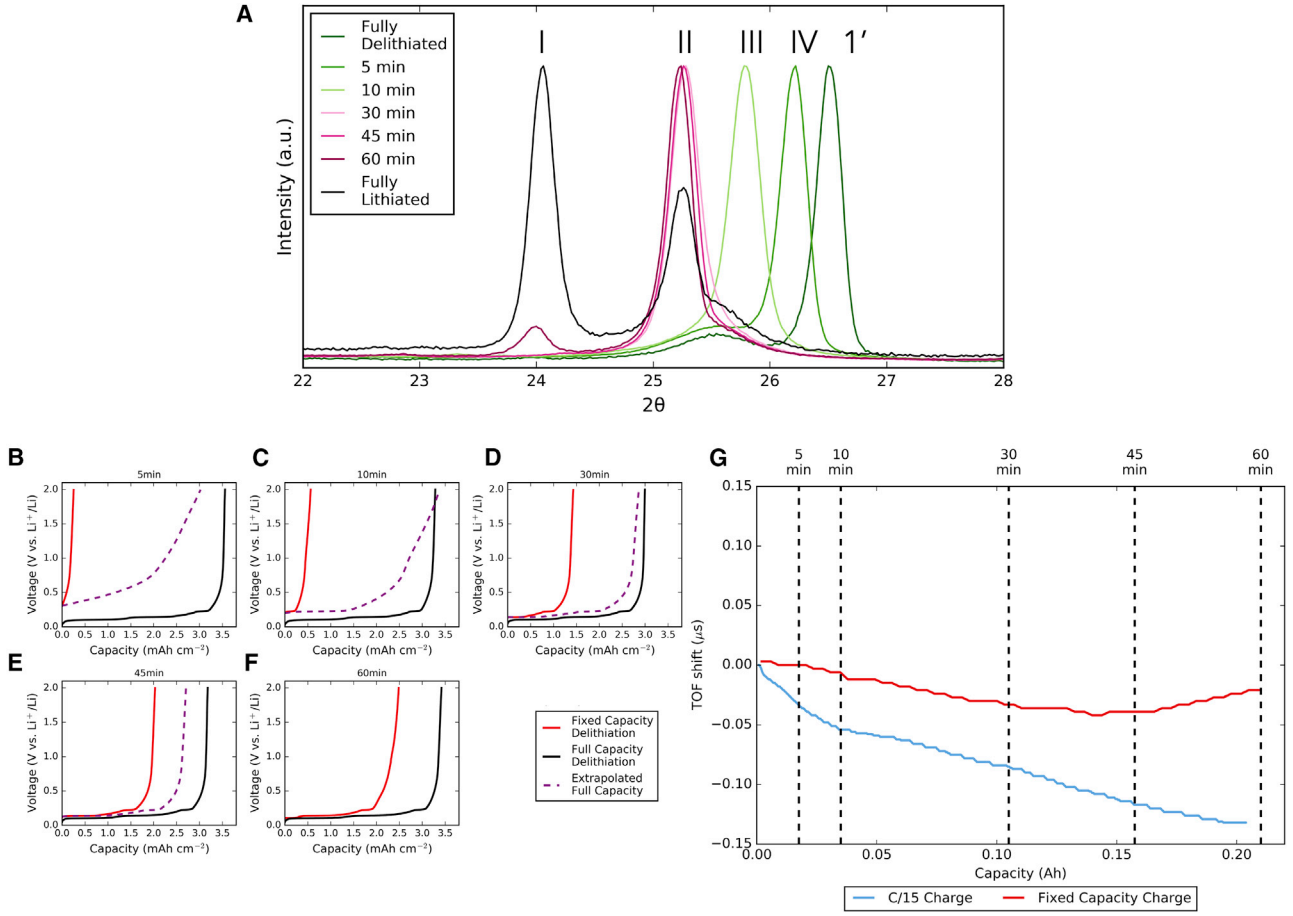

Figure 7. Proof of Concept into Li Metal Plating Mechanism

(A) XRD measurements focused on the (002) peak of the graphite anodes subjected to a partial fixed-capacity charge. Voltage versus capacity plots of partial fixed-capacity delithiation and full-capacity delithiation. The purple curve is the extrapolated value, providing an estimate of what capacity should be if the partial capacity charge scaled linearly.

(B–G) The plots are for partial fixed-capacity charges of (B) 5 min, (C) 10 min, (D) 30 min, (E) 45 min, and (F) full fixed-capacity charge; (G) plot comparing TOF shifts for the cell subjected to a 0°C—1C fixed-capacity charge.

frequency typically upshifts on charge, as shown in the last subplot of each figure. However, rather than upshifting, as it does for the non-plating case, it downshifts for the plated cell. In other words, a slightly lower frequency wave is received by the transducer for the plated cell, which may be due to attenuation from plating. This downshift is observed in the FFT maps for all the plated cell conditions and at the beginning of the plating charge. Therefore, the TOF shift reversal originates from this 2.5-MHz frequency shifting in the opposite direction than typically observed. Further work is in progress on investigating the correlation between wave frequency and actual physical dynamics of the cell.

One drawback of the technique as it currently stands is the bulk methodology. A simple ultrasonic pulse through the length of the battery allows for a quick assessment of the entire stack. At the same time, it also convolutes contributions from individual electrodes. Therefore, it would be difficult to distinguish whether plating occurred on only one or several electrodes and determine which electrodes plated. The acoustic effects are solely based on the area between the transducers, so to identify spatial heterogeneities, multiple transducers can be placed on a single

cell, given that it is large enough. This makes for useful commercial cell quality analysis, especially owing to the low cost and speed at which diagnostics can be carried out. This said, over larger format pouch cells, *areal* inhomogeneities are able to be resolved, as illustrated by previous work.[50] Additionally, because the wavelength of the ultrasonic pulse is relatively low, on the order of ~1 mm, there may exist a minimum resolution beyond which plating cannot be detected (e.g., single-layer electrode pouch cells). Lastly, the sensitivity is also related to the attenuating properties of the media. Form factors that include materials that have higher impedance mismatch with the transducers or that intensify waveform convolution (e.g., springs/spacers in coin cells) may be more difficult to analyze.

In this work, we demonstrate that acoustic measurements can be reliably used to provide strong evidence of Li metal plating within commercial-scale LCO/graphite pouch cells during operation. Specifically, the TOF endpoint difference, defined by the acoustic TOF shift between the top of charge of a slow charge and the top of charge of a faster plating-inducing charge, is shown to be a promising parameter for determining the degree of Li metal plating in the region of the battery connected to the acoustic transducers. This was demonstrated by confirming the degree of lithiation and plating with *ex situ* XRD characterization, optical and microscopic observations, and half-cell electrochemical analysis of the cells that had been subjected to a combinatorial array of test conditions spanning different current rates and temperatures. Using this technique, we are then able to show the existence of an Arrhenius relationship between Li metal plating, current rate, and temperature. We determine that there are statistically significant linear relationships between ultrasonic TOF/graphite staging and ultrasonic TOF/*post mortem* electrochemical measurements, from which we estimate an amount of Li plating. Further, a proof of concept was demonstrated to indicate the possibility of detecting the degree of plating within a single SOC via deviations of the TOF endpoint difference.

These results improve the ability to understand and characterize Li metal plating behavior in commercial LIBs during operation, without the need for custom-made cells or time-consuming and destructive *ex situ* characterization methods. Further refinement of the acoustic data is in progress in order to explore the potential for fully quantitative capabilities. Lastly, this demonstrated capability of acoustic ultrasound to detect Li metal plating opens up a new pathway for *in operando* detection of Li metal and other metal-based battery chemistries.

EXPERIMENTAL PROCEDURES

Electrochemical Cycling of Full Cells

Batteries used were Li-ion 651628 (LCO/graphite) pouch cells, rated for 210 mAh and obtained from AA Portable Power Corp. (BatterySpace). Detailed chemical composition information is shown in Table 1, accessed from the company specification sheet (https://www.batteryspace.com/prod-specs/MSDS/2019/SDS-LiCoO2-2019.pdf).

Cell properties in Table 2 were obtained by reverse engineering a fresh cell at the bottom of discharge. There were 30 cathode (LCO) electrodes and 32 anode (graphite) electrodes, with each electrode being double sided. The LCO electrodes were sonicated in N-methyl-2-pyrrolidone (NMP), and the graphite electrodes were sonicated in deionized (DI) water. The slurry was dried in the vacuum oven at 150°C overnight in order to obtain the dried powder. The weight of the powder was

Table 1. Chemical Composition

Chemical Name	Content (wt%)	CAS Index No.
Lithium cobalt oxide	50	12190-79-3
Graphite	10	7782-42-5
Polypropylene	5	9003-07-0
PVDF	2	24937-79-9
Polyethylene	5	9002-88-4
Carboxymethylcellulose	0.5	9004-32-4
Lithium hexafluorophosphate	5	21324-40-3
Ethylene carbonate	5	96-49-1
Dimethylcarbonate	5	616-38-6
Nickel	2.5	7440-02-0
Copper	5	7440-50-8
Aluminum	5	7429-90-5

measured to obtain the loading (mg/cm^2) and density (g/cm^3). Areal capacity was obtained using the theoretical capacity of 274 mAh/g for LCO and 372 mAh/g for graphite. Brunauer-Emmett-Teller (BET) measurements (Micromeritics ASAP 2020 HV) were taken for both the LCO and graphite in order to obtain the BET surface area and micropore volume.

Batteries were cycled on a Neware BTS3000 cycler and temperature controlled by a thermal incubator (IVYX Scientific) and monitored live via wireless controllers (Particle Photon). All batteries utilized four-wire connectivity to the Neware battery cycler. Cells were cycled at temperatures of 0°C–60°C in 10°C increments. For data collection, cells were cycled twice at a current rate of C/15 between 2.7 V and 4.2 V. Following these two initial cycles, the cells were then charged at a given current rate with a time cutoff, as opposed to a voltage cutoff, to determine whether plating had been induced.

Acoustic Monitoring

The acoustic signal was transmitted and received by a pair of 2.25-MHz transducers (SIUI) that were contacted across the cell. The cell was held in place by a 3D printed holder (Formlabs). The TOF shift is obtained by comparing individual waveforms collected during battery cycling to a reference waveform obtained when the battery was fully discharged (Figure S4), referred to as 0% SOC.

Cell Tear Down and Materials Characterization

Following the plating step, the 210-mAh cells were brought into an argon-filled glovebox before being disassembled to harvest the graphite anodes for materials characterization. The cells were taken apart in a fully charged state to be able to characterize the degree of staging (e.g., lithiation) in the graphite. Furthermore, the cells had an idle period of at least 24 h prior to being disassembled, to allow diffusion of Li metal into the bulk graphite.[28] Optical images of the charged anodes were also taken in the glovebox.

SEM Measurements

SEM images were taken with a Verios 460 XHR with a working distance of 4 mm and accelerating voltage of 5 keV. Samples were rinsed in dimethyl carbonate (DMC) and

Table 2. Cell Properties

	Electrode	No. Layers	Thickness (μm)	Loading (mg/cm^2)	Density (g/cm^3)
LCO	cathode	30	58	8.9	1.54
Graphite	anode	32	66	7.0	1.06

	Capacity (mAh/cm^2)		BET Surface Area (m^2/g)		BET Micropore Volume (cm^3/g)
LCO	2.44		2.45		0.000753
Graphite	2.60		3.18		0.000214

dried in the large vacuum antechamber of the argon-filled glovebox at 40°C for 2 h before imaging. Samples were transferred to the imaging room in sealed containers and exposed to air for less than 5 s, using a vacuum load lock for near-instant pump down.

XRD Measurements

Ex situ XRD measurements were done using a Bruker Discover D8 X-Ray Diffractometer. Anode samples were prepared in an argon-filled glovebox and were protected from ambient air during transfer and measurement with transparent scotch tape. Measurements were taken from 10° to 80° 2θ with a scan rate of $1° \text{ min}^{-1}$.

Half-Cell Electrochemical Cycling

In addition to characterizing the graphite from the opened cells, graphite anodes from each cell condition were also harvested for cycling in Li metal half-cells. The coin cells used were type 2032 cells, with a harvested graphite electrode, 1M $LiPF_6$ EC:DMC electrolyte (Sigma-Aldrich), with a dual polypropylene (Celgard) and glass fiber (Whatman) separator. For cycling, the graphite in the half-cell was first fully delithiated at a current rate of 40 μA cm^{-2} (0.05 mA), before being cycled 10 times at a current rate of 790 μA cm^{-2} (1 mA), and then with two cycles at 80 μA cm^{-2} (0.1 mA). The last two cycles were done at 0.1 mA, as experiments showed negligible differences between latter cycles conducted at 40 μA cm^{-2} and 80 μA cm^{-2}. The cycling was done between 0.01 V and 2 V versus Li^+/Li.

Data and Code Availability

All data associated with the study are included in the paper and the supplemental information. Additional information is available from the corresponding author upon reasonable request.

SUPPLEMENTAL INFORMATION

Supplemental Information can be found online at https://doi.org/10.1016/j.xcrp.2020.100035.

ACKNOWLEDGMENTS

G.D. was supported in part by a generous gift from Ford Motor Company. G.D. was supported in from the Vehicle Technologies Office of the U.S. Department of Energy's Office of Energy Efficiency and Renewable Energy under the guidance of the Advanced Battery Cell Research Program eXtreme Fast Charge Cell Evalulation of Lithium Ion Batteries (XCEL). C.B. and W.C. were supported by Mercedes Benz Research and Development North America. M.W. was supported by a fellowship from the Gates Foundation. The authors acknowledge the use of Princeton's Imaging and Analysis Center, which is partially supported by the Princeton Center for

Complex Materials, a National Science Foundation (NSF)-MRSEC program (DMR-1420541).

AUTHOR CONTRIBUTIONS

D.S., C.B., and W.C. conceived the idea and developed methodology. C.B. and W.C. performed experiments and wrote the manuscript. Y.L. and J.Y. aided with cell tear down and data collection. G.D. and R.M. provided useful discussions on the acoustic technique. M.W. aided with obtaining cell properties. D.S. supervised the project.

DECLARATION OF INTERESTS

D.S. co-founded and has equity in Feasible Corporation, which is commercializing ultrasonic tools for battery quality analysis. Other authors have no competing interests.

Received: August 5, 2019
Revised: February 3, 2020
Accepted: February 19, 2020
Published: April 1, 2020

REFERENCES

1. Fathi, R., Burns, J.C., Stevens, D.A., Ye, H., Hu, C., Jain, G., Scott, E., Schmidt, C., and Dahn, J.R. (2014). Ultra high-precision studies of degradation mechanisms in aged $LiCoO_2$/graphite Li-ion cells. J. Electrochem. Soc. *161*, A1572–A1579.

2. Sarasketa-Zabala, E., Aguesse, F., Villarreal, I., Rodriguez-Martinez, L.M., López, C.M., and Kubiak, P. (2015). Understanding lithium inventory loss and sudden performance fade in cylindrical cells during cycling with deep-discharge steps. J. Phys. Chem. C *119*, 896–906.

3. Anseán, D., Dubarry, M., Devie, A., Liaw, B.Y., García, V.M., Viera, J.C., and González, M. (2017). Operando lithium plating quantification and early detection of a commercial $LiFePO_4$ cell cycled under dynamic driving schedule. J. Power Sources *356*, 36–46.

4. Yang, X.-G., Leng, Y., Zhang, G., Ge, S., and Wang, C.-Y. (2017). Modeling of lithium plating induced aging of lithium-ion batteries: transition from linear to nonlinear aging. J. Power Sources *360*, 28–40.

5. Schindler, S., and Danzer, M.A. (2017). A novel mechanistic modeling framework for analysis of electrode balancing and degradation modes in commercial lithium-ion cells. J. Power Sources *343*, 226–236.

6. Kang, B., and Ceder, G. (2009). Battery materials for ultrafast charging and discharging. Nature *458*, 190–193.

7. Fleischhammer, M., Waldmann, T., Bisle, G., Hogg, B.-I., and Wohlfahrt-Mehrens, M. (2015). Interaction of cyclic ageing at high-rate and low temperatures and safety in lithium-ion batteries. J. Power Sources *274*, 432–439.

8. Waldmann, T., Wilka, M., Kasper, M., Fleischhammer, M., and Wohlfahrt-Mehrens, M. (2014). Temperature dependent ageing mechanisms in lithium-ion batteries – a post-mortem study. J. Power Sources *262*, 129–135.

9. Cano, Z.P., Banham, D., Ye, S., Hintennach, A., Lu, J., Fowler, M., and Chen, Z. (2018). Batteries and fuel cells for emerging electric vehicle markets. Nat. Energy *3*, 279–289.

10. Spingler, F.B., Wittmann, W., Sturm, J., Rieger, B., and Jossen, A. (2018). Optimum fast charging of lithium-ion pouch cells based on local volume expansion criteria. J. Power Sources *393*, 152–160.

11. Liu, Q.Q., Xiong, D.J., Petibon, R., Du, C.Y., and Dahn, J.R. (2016). Gas evolution during unwanted lithium plating in Li-ion cells with EC-based or EC-free electrolytes. J. Electrochem. Soc. *163*, A3010–A3015.

12. Burns, J.C., Stevens, D.A., and Dahn, J.R. (2015). In-situ detection of lithium plating using high precision coulometry. J. Electrochem. Soc. *162*, A959–A964.

13. Ellis, L.D., Allen, J.P., Hill, I.G., and Dahn, J.R. (2018). High-precision coulometry studies of the impact of temperature and time on SEI formation in Li-ion cells. J. Electrochem. Soc. *165*, A1529–A1536.

14. Smith, A.J., Burns, J.C., and Dahn, J.R. (2011). High-precision differential capacity analysis of $LiMn_2O_4$/graphite cells. Electrochem. Solid-State Lett. *14*, A39–A41.

15. Smith, A.J., and Dahn, J.R. (2012). Delta differential capacity analysis. J. Electrochem. Soc. *159*, A290–A293.

16. Petzl, M., and Danzer, M.A. (2014). Nondestructive detection, characterization, and quantification of lithium plating in commercial lithium-ion batteries. J. Power Sources *254*, 80–87.

17. Han, X., Ouyang, M., Lu, L., Li, J., Zheng, Y., and Li, Z. (2014). A comparative study of commercial lithium ion battery cycle life in electrical vehicle: aging mechanism identification. J. Power Sources *251*, 38–54.

18. Bloom, I., Jansen, A.N., Abraham, D.P., Knuth, J., Jones, S.A., Battaglia, V.S., and Henriksen, G.L. (2005). Differential voltage analyses of high-power, lithium-ion cells: 1. technique and application. J. Power Sources *139*, 295–303.

19. Uhlmann, C., Illig, J., Ender, M., Schuster, R., and Ivers-Tiffée, E. (2015). In situ detection of lithium metal plating on graphite in experimental cells. J. Power Sources *279*, 428–438.

20. Bugga, R.V., and Smart, M.C. (2010). Lithium plating behavior in Lithium-ion cells. ECS Trans. *25*, 241–252.

21. Downie, L.E., Krause, L.J., Burns, J.C., Jensen, L.D., Chevrier, V.L., and Dahn, J.R. (2013). In situ detection of lithium plating on graphite electrodes by electrochemical calorimetry. J. Electrochem. Soc. *160*, A588–A594.

22. Forouzan, M.M., Mazzeo, B.A., and Wheeler, D.R. (2018). Modeling the effects of electrode microstructural heterogeneities on Li-ion battery performance and lifetime. J. Electrochem. Soc. *165*, A2127–A2144.

23. Bhattacharyya, R., Key, B., Chen, H., Best, A.S., Hollenkamp, A.F., and Grey, C.P. (2010). In situ NMR observation of the formation of metallic lithium microstructures in lithium batteries. Nat. Mater. *9*, 504–510.

24. Chandrashekar, S., Trease, N.M., Chang, H.J., Du, L.S., Grey, C.P., and Jerschow, A. (2012). ^{7}Li MRI of Li batteries reveals location of microstructural lithium. Nat. Mater. *11*, 311–315.

25. Chang, H.J., Ilott, A.J., Trease, N.M., Mohammadi, M., Jerschow, A., and Grey, C.P. (2015). Correlating microstructural lithium metal growth with electrolyte salt depletion in

lithium batteries using ^{7}Li MRI. J. Am. Chem. Soc. *137*, 15209–15216.

26. Chang, H.J., Trease, N., Ilott, A., Zeng, D., Du, L.S., Jerschow, A., and Grey, C. (2015). Investigating Li microstructure formation on Li anodes for lithium batteries by in situ ^{6}Li/^{7}Li NMR and SEM. J. Phys. Chem. C *119*, 16443–16451.

27. von Lüders, C., Zinth, V., Erhard, S.V., Osswald, P.J., Hofmann, M., Gilles, R., and Jossen, A. (2017). Lithium plating in lithium-ion batteries investigated by voltage relaxation and in situ neutron diffraction. J. Power Sources *342*, 17–23.

28. Zinth, V., von Lüders, C., Hofmann, M., Hattendorff, J., Buchberger, I., Erhard, S., Rebelo-Kornmeier, J., Jossen, A., and Gilles, R. (2014). Lithium plating in lithium-ion batteries at sub-ambient temperatures investigated by in situ neutron diffraction. J. Power Sources *271*, 152–159.

29. Waldmann, T., Hogg, B.I., and Wohlfahrt-Mehrens, M. (2018). Li plating as unwanted side reaction in commercial Li-ion cells – a review. J. Power Sources *384*, 107–124.

30. Waldmann, T., and Wohlfahrt-Mehrens, M. (2017). Effects of rest time after Li plating on safety behavior—ARC tests with commercial high-energy 18650 Li-ion cells. Electrochim. Acta *230*, 454–460.

31. Hsieh, A.G., Bhadra, S., Hertzberg, B.J., Gjeltema, P.J., Goy, A., Fleischer, J.W., and Steingart, D.A. (2015). Electrochemical-acoustic time of flight: *in operando* correlation of physical dynamics with battery charge and health. Energy Environ. Sci. *8*, 1569–1577.

32. Gold, L., Bach, T., Virsik, W., Schmitt, A., Müller, J., Staab, T.E.M., and Sextl, G. (2017). Probing lithium-ion batteries' state-of-charge using ultrasonic transmission – concept and laboratory testing. J. Power Sources *343*, 536–544.

33. Davies, G., Knehr, K.W., Tassell, B.V., Hodson, T., Biswas, S., Hsieh, A.G., and Steingart, D.A. (2017). State of charge and state of health estimation using electrochemical acoustic time of flight analysis. J. Electrochem. Soc. *164*, A2746–A2755.

34. Knehr, K.W., Hodson, T., Bommier, C., Davies, G., Kim, A., and Steingart, D.A. (2018). Understanding full-cell evolution and non-chemical electrode crosstalk of Li-ion batteries. Joule *2*, 1146–1159.

35. Bommier, C., Chang, W., Li, J., Biswas, S., Davies, G., Nanda, J., and Steingart, D. (2020). Operando acoustic monitoring of SEI formation and long-term cycling in NMC/SiGr composite pouch cells. J. Electrochem. Soc. *167*, 020517.

36. Zhang, S.S., Xu, K., and Jow, T.R. (2002). Low temperature performance of graphite electrode in Li-ion cells. Electrochim. Acta *48*, 241–246.

37. Wang, C.Y., Zhang, G., Ge, S., Xu, T., Ji, Y., Yang, X.G., and Leng, Y. (2016). Lithium-ion battery structure that self-heats at low temperatures. Nature *529*, 515–518.

38. Carter, R., and Love, C.T. (2018). Modulation of lithium plating in Li-ion batteries with external thermal gradient. ACS Appl. Mater. Interfaces *10*, 26328–26334.

39. Vladišauskas, A., and Jakevičius, L. (2004). Absorption of ultrasonic waves in air. Ultragarsas *1*, 46–49.

40. Chang, W., Bommier, C., Fair, T., Yeung, J., Patil, S., and Steingart, D. (2020). Understanding adverse effects of temperature shifts on Li-ion batteries: an operando acoustic study. J. Electrochem. Soc. *167*, 090503.

41. Cheng, E., Taylor, N., Wolfenstine, J., and Sakamoto, J. (2017). Elastic properties of lithium cobalt oxide ($LiCoO_2$). J. Asian Ceramic Soc. *5*, 113–117.

42. Marsden, B., Mummery, A., and Mummery, P. (2018). Modelling the coefficient of thermal expansion in graphite crystals: implications of lattice strain due to irradiation and pressure. Proc. Math. Phys. Eng. Sci. *474*, 20180075.

43. Tang, M., Albertus, P., and Newman, J. (2009). Two-dimensional modeling of lithium deposition during cell charging. J. Electrochem. Soc. *156*, A390–A399.

44. Fong, R., von Sacken, U., and Dahn, J.R. (1990). Studies of lithium intercalation into carbons using nonaqueous electrochemical cells. J. Electrochem. Soc. *137*, 2009–2013.

45. Takami, N., Satoh, A., Hara, M., and Ohsaki, T. (1995). Structural and kinetic characterization of lithium intercalation into carbon anodes for secondary lithium batteries. J. Electrochem. Soc. *142*, 371–379.

46. Levi, M.D., Levi, E.A., and Aurbach, D. (1997). The mechanism of lithium intercalation in graphite film electrodes in aprotic media. Part 2. Potentiostatic intermittent titration and in situ XRD studies of the solid-state ionic diffusion. J. Electroanal. Chem. *421*, 89–97.

47. Winter, M., Novák, P., and Monnier, A. (1998). Graphites for lithium-ion cells: the correlation of the first-cycle charge loss with the Brunauer-Emmett-Teller surface area. J. Electrochem. Soc. *145*, 428–436.

48. Gallagher, K.G., Dees, D.W., Jansen, A.N., Abraham, D.P., and Kang, S.-H. (2012). A volume averaged approach to the numerical modeling of phase-transition intercalation electrodes presented for Li_xC_6. J. Electrochem. Soc. *159*, A2029–A2037.

49. Cañas, N.A., Einsiedel, P., Freitag, O.T., Heim, C., Steinhauer, M., Park, D.-W., and Friedrich, K.A. (2017). *Operando* X-ray diffraction during battery cycling at elevated temperatures: a quantitative analysis of lithium-graphite intercalation compounds. Carbon *116*, 255–263.

50. Robinson, J.B., Maier, M., Alster, G., Compton, T., Brett, D.J.L., and Shearing, P.R. (2019). Spatially resolved ultrasound diagnostics of Li-ion battery electrodes. Phys. Chem. Chem. Phys. *21*, 6354–6361.